From Brittle to Ductile: A Structure Dependent Ductility of Diamond Nanothread

Haifei Zhan, Gang Zhang, Vincent BC Tan, Yuan Cheng, John M. Bell, Yong-Wei Zhang, and Yuantong Gu

Supporting Information

S1. The interatomic potentials for the diamond nanothread (DNT)

Currently, there are several available potentials for the carbon-based system. Prior to probing the mechanical properties of DNT, we have compared three commonly used potentials, including the AIREBO potential,[1] the ReaxFF potential,[2] and a representative consistent force filed, i.e., the polymer consistent force field (PCFF, which is commonly used to describe the atomic interactions within the polymer).[3]

As illustrated in Figure S1a, all three potentials predict a similar radial distribution function (RDF), $g(r)$. As is seen, the nearest-neighbor carbon-carbon distance approximates to 1.52 Å sp^3 bonds for all three potentials, which matches with the experimental measurements.[4] The dominant peak at approximately 1.1 Å corresponds to the C-H bonds, with the successive peaks arisen from the second nearest C-C, C-H and H-H correlations.

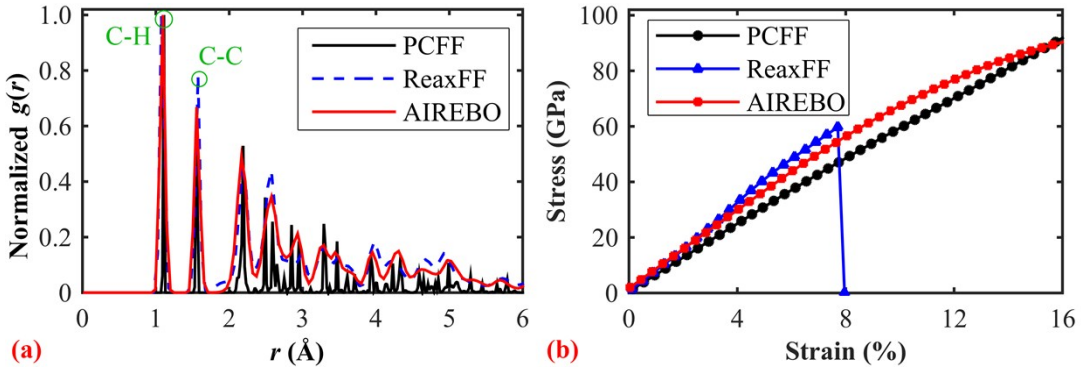

Figure S1 (a) The radial distribution functions for DNT-8 obtained from PCFF, ReaxFF and AIREBO potentials, for the DNT-8 (length ~ 24 nm) after 1 ns relaxation under 300 K (b) The stress-strain curve of the DNT-8 as obtained from different atomic potentials (at 300 K).

Figure S1b compares the stress-strain curves obtained from tensile deformation. Generally, the AIREBO and ReaxFF potential predict a nearly overlapped elastic deformation of the DNT, though a commonly observed spuriously high tensile stress is detected for the AIREBO potential. The ReaxFF potential predicts a yield strength and yield strain around 60 GPa and 7.7%, respectively. In comparison, the PCFF

potential shows a softer behavior, and a similar spuriously high tensile stress as observed from AIREBO potential is also appeared. Specifically, the estimated Young's modulus (within strain < 4%) from AIREBO and ReaxFF potential are about 782 and 795 GPa, respectively, about 25% larger than that extracted from the PCFF potential (~ 628 GPa).

Above results suggest that both PCFF and AIREBO potentials suffer from certain deficiency in describing the tensile properties of DNT. However, although ReaxFF potential yields to a more reasonable result, its complexity requires large computational resources and impedes easy combination with other atomic potentials (for DNT-based potential nanostructures, e.g., DNT-enforced nanocomposites). Thus, the AIREBO potential is usually a preferential choice for larger-scale MD simulation for carbon-based nanomaterials or nanostructures. Although there is rare discussion on the nonphysical high tensile stress produced by the PCFF potential, an effective modification to avoid such phenomenon from AIREBO potential has already been widely used in literature. Basically, the nonphysical high tensile stress phenomenon is originated from the fixed switching function as implemented in the AIREBO potential (between 1.7 and 2.0 Å), which is given as:

$$f = \begin{cases} 1, & r_{ij} < rc_{\min} \\ \left\{1 + \cos\left[\dfrac{\pi(r_{ij} - rc_{\min})}{(rc_{\max} - rc_{\min})}\right]\right\}/2, & rc_{\min} < r_{ij} < rc_{\max} \\ 0, & rc_{\max} < r_{ij} \end{cases}$$

where $rc_{\min}$ and $rc_{\max}$ correspond to the cut-off radii, which are 1.7 and 2.0 Å, respectively. The values are defined based on the first and the second nearest neighbouring distances of the relevant hydrocarbon. The switching function is supposed to significantly influence the forces in the vicinity of the inflection point.[5] To overcome such problematic issue, the original 1.7 Å is usually extended far beyond the inflection point (ranging from 1.9 to 2.0 Å).

To find a reasonable cut-off distance ($rc_{\min}$) for the DNT, the results obtained from the ReaxFF potential were taken as a benchmark. Figure S2a compares the stress-strain curves as obtained by changing the cut-off distance of the AIREBO potential from 1.9 to 2.0 Å. With varying $rc_{\min}$, the elastic deformation of the DNT (the

overlapped portion of the stress-strain curves) appears unchanged. However, the yield strain (together with the yield strength) receives a significant reduction when the cut-off distance increases from 1.9 to 2.0 Å. For instance, for $rc_{\min} = 1.9$ Å, the yield strain ε_y is about 20.5%, which is over four times of that obtained from the $rc_{\min} = 2.0$ Å ($\varepsilon_y \sim$ 4.4%). Similarly, the yield strength for $rc_{\min} = 1.9$ Å is about 89 GPa, which corresponds to more than two times of that obtained from the $rc_{\min} = 2.0$ Å ($E_y \sim$ 34 GPa).

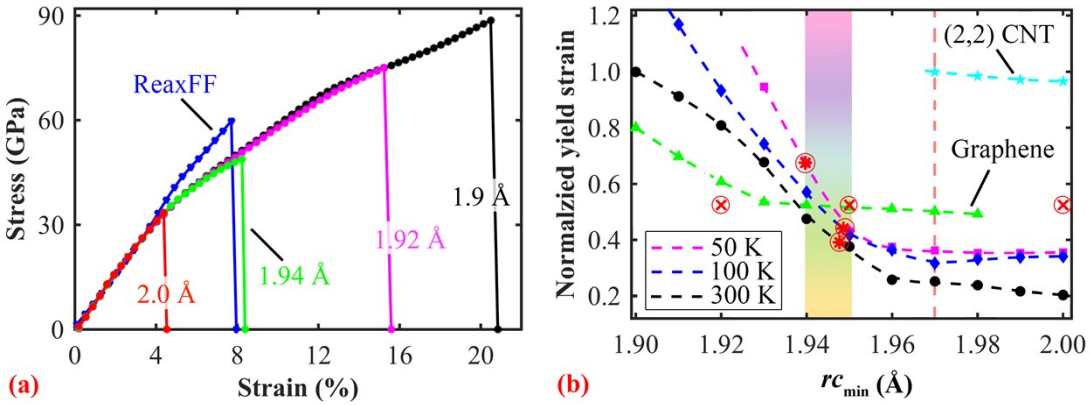

Figure S2 (a) The stress-strain curves of DNT-8 as obtained from ReaxFF potential and AIREBO potential with modified cut-off distance ranging from 1.9 to 2.0 Å at 300 K (sample size of ~ 24 nm). (b) Comparisons of the normalized yield strain under different cut-off distance with varying simulation temperature. The dashed lines are the corresponding spline fitting curves. The circled star markers represent the intersection values between the fitting spline curves and the values obtained from ReaxFF potential. The green triangles are the normalized yield strength obtained from graphene with different cut-off distances,[6] which are normalized by the value at 1.90 Å and shifted 0.2 for comparison clarity. The circled 'X' markers denote three representative cut-off distances that are adopted to study the mechanical properties of graphene-based systems, including 1.92 for irradiated graphene with vacancy;[7] 1.95 for bilayer graphene with sp^3 bonds;[8] and 2.00 for grapheme nanoribbon.[9] The cyan stars are the normalized yield strength for ultra-thin (2,2) CNT.

A series of testings have been carried out to further illustrate the impacts from the cut-off distance of the AIREBO potential. Taking the DNT-8 as a representing system, Figure S2b compares how the normalized yield strain changes while the cut-off distance increases from 1.90 to 2.0 Å at 300 K (the black dashed line). Note that the change of the cut-off distance is directly related with the bond breaking during tension, i.e., the $rc_{\min}$ directly determines the yield strain. Thus, we focus on the change of yield strain though the associated change of the yield strength shares a similar pattern. Generally, the yield strain receives a sharp reduction until the cut-off

distance increases to around 1.96 Å, afterwards, it saturates to a certain value (which is only around 20% of that extracted from $rc_{\min} = 1.9$ Å). A similar changing profile has also been observed from the testing under temperatures of 200, 100 and 50 K as compared in Figure S2b. Note that the results from 200 K are not presented for the sake of comparison clarity. Referring to the results from ReaxFF potential, the intersection value suggests that a cut-off distance between 1.94 - 1.95 Å would result in a comparable yield strain by using AIREBO potential, which shows marginal dependency on the temperature. In summary, above results suggest that the mechanical properties (except Young's modulus) of the DNT relies heavily on the selection of the cut-off distance while using AIREBO potential, particularly when it is smaller than ~ 1.96 Å. To compare with the results obtained from ReaxFF potential, a 1.945 Å is suggested for $rc_{\min}$ from 50 to 300 K, which was used in our simulations.

Of interest, we also summarized the cut-off distance being adopted for the two classes of carbon-based nanostructures in Table S1, i.e., graphene-based and CNT-based systems. For graphene, a recent study suggested that the cut-off distance should be chosen from 1.92 to 2.0 Å.[6] As compared in Figure S3b, the normalized yield strength starts to converge when $rc_{\min}$ is larger than ~ 1.93 Å. For CNT, we have simulated the tensile deformation of (2,2), (5,0) and (7,0) CNTs with cut-off distance ranging from 1.90 to 2.00 Å (under 300 K) as such a comparison is lacking in literature. It is found that the spuriously high tensile stress disappears only until the cut-off distance reaches ~ 1.97 Å, and the yield strain exhibits much less difference for various $rc_{\min}$ values (comparing with that of the DNT). As shown in Figure S3, the yield strength of the ultra-thin (2,2) CNT receives a reduction within 10%, with the larger CNTs experiencing less than 20% reduction. Above results signify that the carbon-based systems have different sensitivities to the selection of cut-off distance. Such different sensitivities may originate from various reasons. Considering the intrinsic differences between various nanostructures, the carbon hybridization state and the geometrical structure and size are regarded as the major contributors. It is also suggested that although the cut-off distance barely influences the interpretation of Young's modulus, a big difference might occur to the yield strain/strength. Thus, comparisons of the mechanical properties between different carbon-based systems using AIREBO potential should be made cautiously with regards to this potential divergence. Unfortunately, though the tensile properties of carbon-based nanostructures with

various carbon hybridization states (sp^1, sp^2 and sp^3) have been accessed (see Table S1), a discussion on how the selection of the cut-off distance would impact the results is generally missing. However, such a discussion is beyond the focus of our current paper, same as seeking a proper solution to permanently avoid this cut-off distance issue. Plenty of trivial works together with first principle calculations are still needed in this regard.

Table S1 A summary of the cut-off distance of the AIREBO potentials being used for various carbon-based systems. Note that there are huge volume of numerical works reporting the tensile properties of carbon-based nanostructures. A complete list is impossible, therefore only some of the representative works have been listed here to illustrate the different carbon-based systems that have been investigated.

	System/nanostructures	Cut-off distance	Remarks
Graphene-based	Irradiated graphene with vacancy[7]	1.92 Å	Tension, 300 K
	Graphene blister simulation[10]	1.95 Å	Coating & folding
	Graphene with SW defects[6]	1.95 Å	Tension, 300 K
	Bilayer graphene with sp^3 bonds[8]	1.95 Å	Tension, 1 K
	Bilayer-graphene with sp^3 bonds and surface hydrogenation[11]	2.0 Å	Tension, 300 K
	Graphene nanoribbon[9]	2.0 Å	Tension, 300 K
	Nanocrystalline graphene[12]	2.0 Å	Tension, 300 K
	Polycrystalline graphene with notch[13]	2.0 Å	Tension, 300 K
	Grapene allotrope[14]	2.0 Å	Tension, 300 K
	Graphene allotrope with acetylenic linkages, sp^2+sp^1 hybrids[15]	2.0 Å	Tension & shear
CNT-based	(6,3) CNT[16]	2.0 Å	Tension-twisting, 298.15 K
	Filled CNTs with *n*-butane or nanopeapod[17]	1.95 Å	Tension-torsion, 300 K
	CNT pillared graphene hybrid structure with boron/nitride doping[18]	2.0 Å	Tension, 1 K
	Carbon nanotube 2D network[19] and 3D supertube[20]	2.0 Å	Tension, 300 K
	CNT with defects[21]	2.05 Å	Tension, 10 K

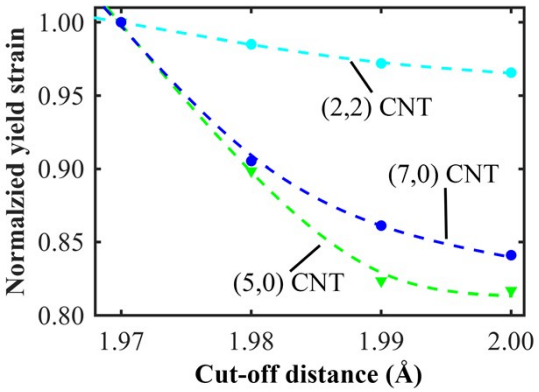

Figure S3 Comparisons of the normalized yield strength among three different single-wall CNTs (sample size ~ 24 nm) at the temperature of 300 K. In all cases, it is found that the spuriously high stress disappears only until the cut-off distance is larger than around 1.97 Å.

S2. The influence from strain rate

To acquire the impacts from strain rate, a 24 nm DNT-17 was considered. Strain rate including 1×10^{-6}, 5×10^{-7}, 1×10^{-7}, 5×10^{-8}, and 1×10^{-8} fs^{-1} were examined.

Figure S4 compares the stress-strain curves under different strain rates. As is seen, the DNT exhibits different yield strength/strain at different strain rates, which is analog to the previous studies on nanowires.[22-24] As expected, higher strain rate leads to larger yield strength/strain. More importantly, it is found that the strain rate has minor impacts when it is lower than $1\times10^{-7}fs^{-1}$ for DNT-17. In-detail analysis show that although the DNT exhibits different yield strength/strain, the deformation mechanisms are the same, i.e., stress concentration at the locations of SW transformation defect and the failure originated from these locations. Overall, our initial results show that the DNT has an obvious strain-rate dependent tensile property at high strain rate. However, to fully unveil such strain-rate-dependency, a further study is required (by isolating the structural and thermal impacts). These results also signify that the strain rate (10^{-7} fs^{-1}) adopted in this work exerts ignorable impacts on the tensile behaviour of the studied DNT, and it is suitable for the investigation purpose.

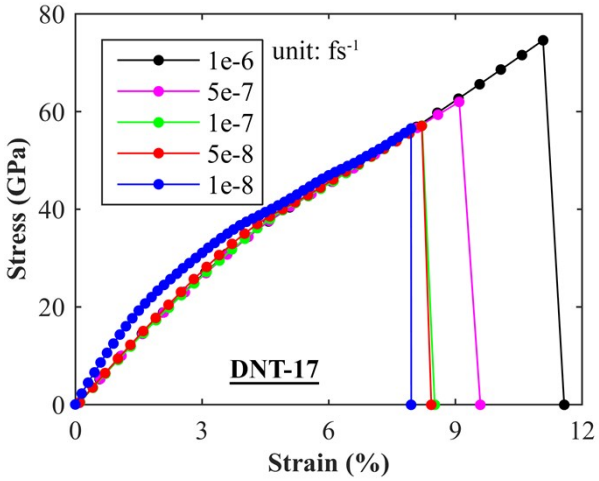

Figure S4 Comparisons of the stress-strain curves under different strain rates for the DNT-17 (sample size ~ 24 nm).

S3. The DNTs with evenly and unevenly distributed SW transformation defects

To elucidate the influence from the locations of SW transformation defectss. Four DNT models with unevenly distributed SW transformations have been examined as shown in Figure S4. A uniform sample length is used for different DNTs.

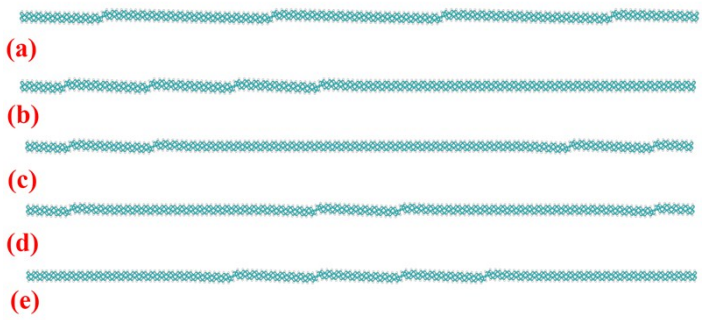

Figure S5 The DNT models with four evenly and unevenly distributed SW defects. All models have periodic boundary conditions along the length direction and an identical size of ~ 31 nm.

Generally, different DNTs exhibit a nearly overlapped elastic deformation as illustrated in Figure S5a. Comparing with the evenly distributed sample, the difference of the estimated Young's modulus is within 1%, indicating an ignorable influence from the location of the SW defect. However, an evident impact on the yield strain/strength is observed. As is seen in Figure S5a, an increment up to ~ 13% and ~ 10% for the yield strength and yield strain is observed, respectively, due to the location change of the SW defect. As compared in Figure S5b, different locations of the SW defect will obviously influence the stress distribution, which introduces stronger local variances, and thus induces different yield strain and yield strength.

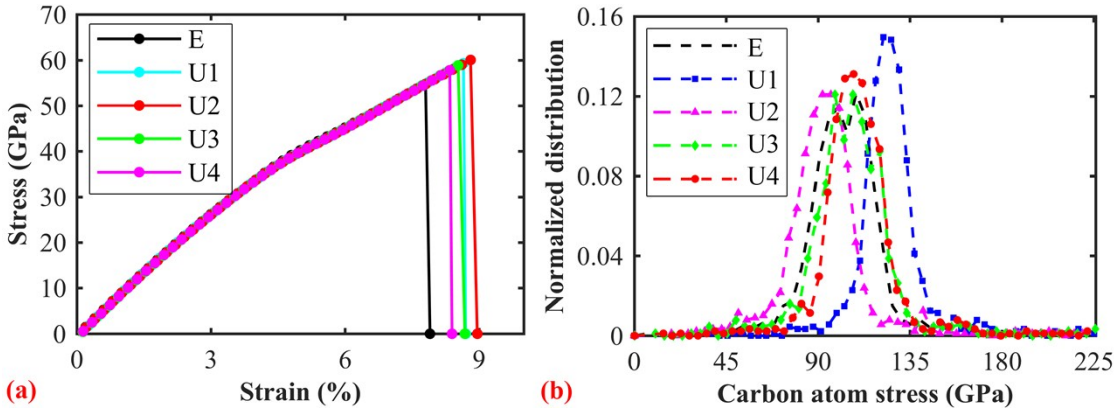

Figure S6 (a) The stress-strain curves as obtained from the DNTs with evenly and unevenly distributed DNTs. (b) The normalized distribution of the virial atomic stress for carbon atoms along the length direction at the strain of 7.5%, showing that the location of the SW defects will influence the stress distribution during tensile deformation and thus make the DNT exhibit different yield strength and yield strain.

S4. The tensile testing for a confined region

For the tensile testing with confined region, the periodic boundary conditions of the model have been switched to free boundary conditions. The irrelevant regions of the DNT have been frozen during the simulation (see Figure S6a). A low constant velocity range has been used to drive the tensile deformation with a time step of 0.0005 ps. Depending on the sample length, the strain rate ranges from 1 to 9.5×10^{-7} fs^{-1}. Recall the results in Figure S2b, a large cut-off distance of 2.0 Å has been used to avoid the nonphysical high stress as induced by the AIREBO potential. As illustrated in Figure S6b, during the first stress increase period, only stretched C-C bonds are observed. When the strain approaches 16%, two C-C bonds of the pentagons start to break, which initiates the hardening process. After failure, the previously broken bond was reformed, which restored the left pentagons (Figure S6d).

By tuning the length of the confined regions with SW defect, we found a gradual transition of the mechanical properties of the SW defect. As shown in Figure S7a and S7b, the yield strain decreases initially sharply and then gradually from 25% to around 5%, and the yield strength decreases similarly but with a smaller reduction amplitude. These results suggest a ductile characteristic of the SW defect. In comparison, the mechanical properties of confined regions with only poly-benzene rings appear irrelevant with the region length, indicating the brittle characteristic of the poly-benzene rings.

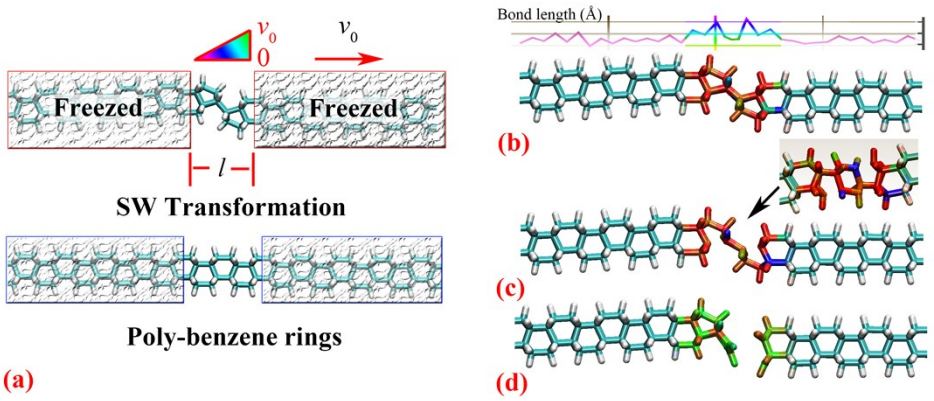

Figure S7 (a) The simulation settings for a confined region. The atomic configurations of the confined region with only the SW defect at the strain of: (b) 7.1%; (c) 16.1% and (d) 24.6%.

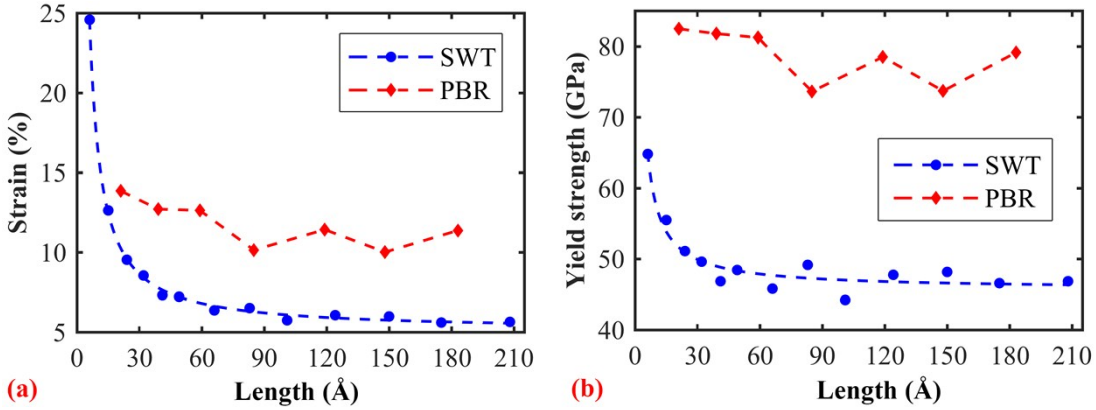

Figure S8 (a) The yield strain as a function of the confined region length; (b) the yield strength as a function of the confined region length.

S5. The fitting results using the serial spring model

Fitting the spring model with the full MD results shows a big divergence between them as illustrated in Figure S8a. Also, the fitting parameters vary greatly from each other (Table S2). Such observation indicates the inappropriateness of the spring model in describing the mechanical behaviour of the DNT. The origin for such inappropriateness is due to the ductile transition of the DNT that is not captured by the spring model. Considering of this, the adjusted fitting using only the data from DNT exhibiting brittle characteristic yields a good agreement. As shown in Figure S8b, the spring model fits well with the MD results from DNTs constructed by larger units (longer than DNT-6). More importantly, the obtained fitting parameters (listed in Table S2) agree well with each other. Therefore, it is concluded that the spring model can be used to describe the brittle DNT, whereas it is unable to give good description for the ductile DNT.

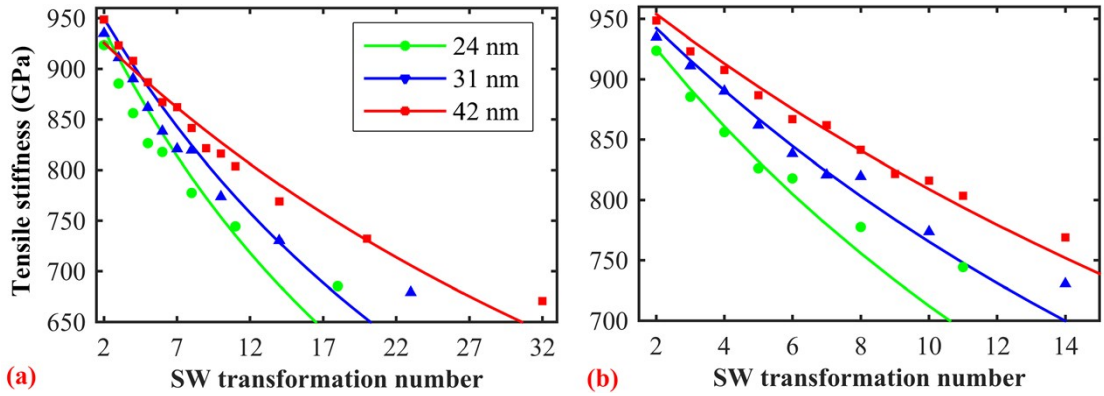

Figure S9 (a) The fitting using all MD results; (b) the adjusted fitting using the data from DNT with constituent units longer than DNT-6.

Table S2 Fitting results based on the serial spring model using the MD results from DNTs with constituent units longer than DNT-6. SWT and PBR represent the SW defect and poly-benzene rings regions, respectively.

Sample length (L, nm)			24	31	42	Roman[25]
Full-range fitting		SWT: Effective length (L_{sw}, nm)	0.29	0.36	10.93	
		SWT: Tensile stiffness (E_{sw}, GPa)	272.5	305	901	
		PBR: Tensile stiffness (E_{pb}, GPa)	1000	1000	954	
Adjusted fitting		SWT: Effective length (L_{sw}, nm)	0.42	0.46	0.39	0.48
		SWT: Tensile stiffness (E_{sw}, GPa)	303.8	326.3	281.1	306-347
		PBR: Tensile stiffness (E_{pb}, GPa)	1000	1000	998.7	1089

References

1. S. J. Stuart, A. B. Tutein and J. A. Harrison, *J. Chem. Phys.*, 2000, **112**, 6472-6486.
2. A. C. Van Duin, S. Dasgupta, F. Lorant and W. A. Goddard, *J. Phys. Chem. A*, 2001, **105**, 9396-9409.
3. H. Sun, S. J. Mumby, J. R. Maple and A. T. Hagler, *J. Am. Chem. Soc.*, 1994, **116**, 2978-2987.
4. T. C. Fitzgibbons, M. Guthrie, E.-s. Xu, V. H. Crespi, S. K. Davidowski, G. D. Cody, N. Alem and J. V. Badding, *Nat. Mater.*, 2015, **14**, 43-47.
5. O. Shenderova, D. Brenner, A. Omeltchenko, X. Su and L. Yang, *Phys. Rev. B*, 2000, **61**, 3877.
6. L. He, S. Guo, J. Lei, Z. Sha and Z. Liu, *Carbon*, 2014, **75**, 124-132.
7. C. Carpenter, D. Maroudas and A. Ramasubramaniam, *Appl. Phys. Lett.*, 2013, **103**, 013102.
8. Y. Y. Zhang, C. M. Wang, Y. Cheng and Y. Xiang, *Carbon*, 2011, **49**, 4511-4517.
9. H. Zhao, K. Min and N. R. Aluru, *Nano Lett.*, 2009, **9**, 3012-3015.
10. X.-Y. Sun, R. Wu, R. Xia and Y.-J. Xu, *RSC Advances*, 2014, **4**, 46646-46652.
11. A. R. Muniz, A. S. Machado and D. Maroudas, *Carbon*, 2015, **81**, 663-677.

12. T. Zhang, X. Li, S. Kadkhodaei and H. Gao, *Nano Lett.*, 2012, **12**, 4605-4610.
13. Z. Sha, Q. Pei, Z. Liu, V. Shenoy and Y. Zhang, *Carbon*, 2014, **72**, 200-206.
14. Y. Y. Zhang, Q. X. Pei and C. M. Wang, *Appl. Phys. Lett.*, 2012, **101**, 081909-081909-081904.
15. J. Zhao, N. Wei, Z. Fan, J.-W. Jiang and T. Rabczuk, *Nanotechnology*, 2013, **24**, 095702.
16. B. Faria, N. Silvestre and J. C. Lopes, *Compos. Sci. Technol.*, 2013, **74**, 211-220.
17. B.-W. Jeong, J.-K. Lim and S. B. Sinnott, *Appl. Phys. Lett.*, 2007, **90**, 023102.
18. K. Xia, H. Zhan, Y. Wei and Y. Gu, *Beilstein Journal of Nanotechnology*, 2014, **5**, 329-336.
19. H. F. Zhan, G. Zhang, J. M. Bell and Y. T. Gu, *Appl. Phys. Lett.*, 2014, **105**, 153105.
20. H. Zhan, J. M. Bell and Y. Gu, *RSC Advances*, 2015, **5**, 48164-48168.
21. M. Sammalkorpi, A. Krasheninnikov, A. Kuronen, K. Nordlund and K. Kaski, *Phys. Rev. B*, 2004, **70**, 245416.
22. A. Koh and H. Lee, *Nano Lett.*, 2006, **6**, 2260-2267.
23. W. Liang and M. Zhou, *Nanotechnology*, 2003, **2**, 452-455.
24. H. Ikeda, Y. Qi, T. Çagin, K. Samwer, W. L. Johnson and W. A. Goddard, *Phys. Rev. Lett.*, 1999, **82**, 2900.
25. R. E. Roman, K. Kwan and S. W. Cranford, *Nano Letters*, 2015.